PHYSICAL REVIEW B **71**, 115425 (2005)

Curvature effects in surface plasmon dispersion and coupling

A. Passian* and R. H. Ritchie
Oak Ridge National Laboratory, Oak Ridge, Tennessee 37831, USA

A. L. Lereu
Université de Bourgogne, Département de Physique, 21011 Dijon, France

T. Thundat and T. L. Ferrell
Oak Ridge National Laboratory, Oak Ridge, Tennessee 37831, USA

(Received 1 July 2004; revised manuscript received 27 October 2004; published 25 March 2005)

We have studied the resonant coupling of surface plasmons in curved thin-film tunneling geometries by obtaining the dispersion relations for the system. The surface plasmon dispersion relations are calculated for a metal-coated dielectric probe above a dielectric half space with and without metal coating. The system is modeled in the prolate spheroidal system, and the dispersion relations are studied as functions of the parameter that defines the boundaries of the tip and the corresponding coating, and as functions of the involved coating thicknesses. Using this type of probe-substrate configuration, the nonradiative surface plasmon coupling mechanism is investigated in the visible spectrum at frequencies relevant to scanning probe microscopy. The simulations of the results predict optical access to the resonant surface modes of the system.

DOI: 10.1103/PhysRevB.71.115425 PACS number(s): 68.37.Ef, 68.37.Uv, 73.20.Mf, 71.45.−d

I. INTRODUCTION

The quanta associated with the waves in bulk matter (plasmons) were discussed in the early 1950s by Bohm and Pines[1] in order to explain the characteristic peaks observed in the energy-loss spectrum of fast electrons penetrating metal foils. The peaks were shown to correspond to plasmon generation in the foil. The quanta associated with the surface waves (surface plasmons) were described in 1957 by Ritchie[2] in order to explain the observation of the reduced energy peaks in the energy-loss spectrum not accounted for by the plasmon concept alone. The observation of multiple discrete energy losses was thus explained by invoking the bulk and surface plasmon concepts.[3] Optical access to the surface plasmons and their susceptibility to the geometric parameters and dielectric properties of the surrounding medium gave rise to a different series of applications, such as sensing and imaging. These applications typically involve excitations of surface plasmons on small metal particles (particle plasmons) or at the interfaces of a thin metal film. For the surface plasmons on a plane-bounded semi-infinite metal, the resonance occurs when the real part of the dielectric function is -1. For a sphere that is small compared to the wavelength, the dipolar resonance condition occurs at the frequency for which the real part of the dielectric function is equal to -2. Even more negative values are obtained for prolate spheroids. In the case of a thin foil, the resonance condition depends on the wave vector κ of the surface plasmon and the foil thickness in a transcendental dispersion relation. If the foil is curved, then its electronic resonances will change. Such variations can be important, for example, in the context of scanning probe microscopy (SPM). The quantum mechanical process of electron tunneling and the phenomenon of photon tunneling associated with the frustrated total internal reflection are the well-known underlying principles of the operation of the scanning tunneling microscope (STM) and the photon scanning tunneling microscope[4] (PSTM). The finite transmitted amplitude in the probe medium determines the amplitude of the acquired signal, which can be greatly influenced by the geometric factors of the probe-substrate system. In the case of collective electronic excitations[5] in metal probes and/or samples, this is closely related to the availability of the resonant modes of the entire system.

Classical nonretarded electrodynamics with a dielectric description of a metal can provide valuable information regarding the possible plasmon modes of a system.[5–7] Within this framework, the dispersion relations are uniquely determined by the material properties and geometric characteristics of the system, and thus can offer important information, in particular, with regard to the optical access to the resonant modes of a supporting medium and their dependence on smooth or unsmooth curvature. For example, it can be shown that the dispersion relation for surface plasmons on a statistically slightly rough surface displays a splitting that can lead to a double peak in the reflection measurement.[8] Another example is the optical excitation of surface plasmons in gold islands, which undergoes spectral variation as a result of reshaping[9] the submicron gold particulates or changing the underlying substrate.[10,11] This can be visually observed as a change in the color of the thin gold film, or spectrally recorded using a spectrophotometer. The discrete surface modes of the gold particulates[12] are responsible for such spectral shifts. Thus, surface modes (as opposed to bulk modes) are strong mediators of size and geometry of the material media, as prescribed by the application of the boundary conditions imposed on the involved electromagnetic fields. For these reasons, dispersion relations have been calculated to various degrees of geometrical complexity for a variety of material domains, such as a slab,[13–15] multiple-film systems,[16,17] metal gratings,[18–20] ionic and metallic spheres,[21] spheroidal particles,[12,22] cones and double cones,[22,23] metallic cylinder,[21,24,25] and metal-coated dielectric cylinder.[26]

Probe-sample interactions and experimental observation of the stimulation and propagation of the surface plasmons in SPM systems have been reported in several works.[27–35] An example can be found in the work of Krenn *et al.*,[33] where optically excited localized surface plasmon coupling between a submicron gold particle and wire was observed using a PSTM. Theoretical models for various SPM probe-sample configurations have been reported where the probe is approximated by a finite body residing close to or in the near field of a substrate. For example, Madrazo *et al.*[36] simulated the probe as a two-dimensional cylinder within a few nanometers above a metal surface with direct illumination. Similarly, González *et al.*[37] reported a study of the optical forces exerted on a metal probe modeled as a two-dimensional silver cylinder above a substrate illuminated via total internal reflection. Recently, Porto *et al.*[38] investigated the interaction of a directly illuminated probe-substrate system by modeling the probe as a metal sphere located a few nanometers above a metal substrate.

In this paper, we study the feasibility of the coupling of surface plasmons in thin metal films and the effect of curvature on such a coupling. We predict optical excitation of this coupling in geometries relevant to the physics of surfaces, nanostructures, and scanning probe microscopy. Such geometries are important when studying the near-field or localized plasmon excitation in submicron particles[39] or field enhancement in surface-enhanced Raman scattering.[40] The geometric effects in the study of interacting thin metallic films at finite interaction distances can also provide useful information when studying the Casimir and Van der Waals forces.[6] In the limit of vanishing film thickness, a closely related example is found in the work of Sernelius and Björk,[41] where the interaction energy for a pair of quantum wells was calculated by treating them as two-dimensional metallic sheets.

Due to analytical difficulties, there is a trade-off between the geometrical complexity with nonretarded approach and geometrical simplification with fully retarded approach. Nevertheless, each approach can offer both quantitative and qualitative information about the system, in particular, with regard to its limiting behavior in the context of dispersion, resonances, and coupling.[6] Here, we present the exact results of the calculation of the dispersion relations for a system composed of a hyperboloidal multilayered medium located above a multilayered Cartesian medium. Section II A is devoted to the description of the solutions of Laplace's equation, whereas in II B the nonretarded dispersion relations are derived within the local response approximation. Numerical work and discussions of the results will be given in Sec. III. Finally, a summary of the conclusions is presented in Sec. IV.

II. DISPERSION RELATIONS

A. Scalar potential of the electric field

We model the curved thin metal film by representing its boundary with the surface of a single-sheeted hyperboloid of revolution. The probe dielectric and the planar thin metal film interfaces are modeled by confocal hyperboloids. The use of such surfaces can be justified computationally by surface-fitting procedures to scanning electron microscope images of a metal-coated probe tip.[42] One of the most important features of employing the spheroidal coordinate system here is the possibility of coexistence of planar boundaries with hyperboloidal surfaces, appropriate for modeling several "probe tip-substrate" configurations present in scanning probe microscopy.[43,44]

The transformation between the Cartesian and the spheroidal systems is performed by[45]

$$x(\zeta,\theta,\varphi) = z_0 \sinh\zeta \sin\theta \cos\varphi,$$

$$y(\zeta,\theta,\varphi) = z_0 \sinh\zeta \sin\theta \sin\varphi,$$

$$z(\zeta,\theta,\varphi) = z_0 \cosh\zeta \cos\theta, \tag{1}$$

in the domain defined by

$$0 \leqslant \zeta < \infty, \quad 0 \leqslant \theta \leqslant \pi, \quad 0 \leqslant \varphi \leqslant 2\pi, \tag{2}$$

with z_0 being an overall scale factor, which also sets the focal points for the hyperboloids defined by fixed θ (or spheroids defined by fixed ζ). In what follows, we will make the variable substitutions $\cosh\zeta = \eta$ with $1 \leqslant \eta < \infty$ and $\cos\theta = \mu$ with $-1 \leqslant \mu \leqslant 1$.

Since the system as a whole is electronically neutral, the scalar potential of the electric field $\Phi(\zeta,\theta,\varphi)$ satisfies Laplace's equation $\Delta\Phi = 0$, which is separable in the spheroidal system.[46] The fully retarded case is complicated in these coordinates, due to the evaluation of radial and angular spheroidal wave functions.[47,48] The general solution can now be expanded as a Fourier series in the azimuthal variable φ as[49]

$$\Phi(\eta,\mu,\varphi) = \sum_{0}^{\infty} f_m(\eta) g_m(\mu)(2-\delta_m^0)\cos m\varphi, \tag{3}$$

where f and g, using the Laplacian in the spheroidal system,[50] and a separation constant c satisfy

$$\frac{d}{d\eta}\left[(\eta^2-1)\frac{df_m(\eta)}{d\eta}\right] - \frac{m^2}{\eta^2-1} f_m(\eta) = c f_m(\eta),$$

$$\frac{d}{d\mu}\left[(1-\mu^2)\frac{dg_m(\mu)}{d\mu}\right] - \frac{m^2}{1-\mu^2} g_m(\mu) = -c g_m(\mu). \tag{4}$$

The possibility of obtaining a continuous spectrum of real eigenvalues and eigenfunctions relies on setting $c = \nu(\nu+1)$, with ν given by the complex number $\nu = -\frac{1}{2} + iq$, resulting in $c = -\frac{1}{4} - q^2$, where q is a real continuous variable $q \in [0,\infty[$. This is appropriate for the infinite surface of a hyperboloid as opposed to the discrete values of ν arising in the case of bounded surfaces, such as those of spheroids where ν is an integer. The particular values of Re $\nu = -\frac{1}{2}$, and Im $\nu = q$ is a consequence of the necessary criteria for existence of the eigenvalues and orthogonal eigenfunctions[51–53] and result in the finiteness of the scalar potential in the interior-exterior boundary value problem in potential theory. The discrete modes of objects with finite volumes, such as an ellipsoid,[12] can be envisioned as standing waves oscillating on the surface of the particle. When one of the dimensions of the system is allowed to be infinite, the corresponding eigenmodes become continuous and this can alter the dispersion relations dramatically and have consequences for the extension of energy localization.

It can be shown[46,54] that Eqs. (4) are solved by the associated Legendre functions with continuous complex lower index (conical functions) $P^m_{-(1/2)+iq}(z)$. The argument $z\in\,]-\infty,\infty[$ is set to $z=\eta$ to give the solution to the first equation in (4), while it takes on $z=\pm\mu=\pm\cos\theta$ to generate the two linearly independent solutions of the second equation in (4). Using the recursion relations for the conical functions, it can be shown that the differential equations in (4) are satisfied by the conical functions. It can be seen, from the asymptotic expansion[51,55,56] of the conical function, in the limit of large argument, that the negative real part of $-1/2$ makes these functions decay. We note that the sum in (3) runs only over positive m due to $P^m_{-(1/2)+iq}(z) = Z^m_q P^{-m}_{-(1/2)+iq}(z)$, where $Z^m_q, m=0,1,2,\ldots$ is defined by the ratio[57] of the Γ functions

$$Z^m_q = \frac{\Gamma\left(\frac{1}{2}+m-iq\right)}{\Gamma\left(\frac{1}{2}-m-iq\right)} = (-1)^m\left(q^2+\frac{1}{4}\right)\left(q^2+\frac{9}{4}\right)\cdots \times\left[q^2+\frac{(2m-1)^2}{4}\right]. \tag{5}$$

Also, with the above value for ν, both $P^m_{-(1/2)+iq}(z)$ and Z^m_q are even in q, consistent with the fact[53] that we do not need to include the region of the eigenvalue spectrum beyond Re $\nu-1$.

The following orthogonality relation[58] for the conical functions with argument $1\leqslant\eta<\infty$:

$$\int_1^\infty P^m_{-(1/2)+iq}(\eta)P^m_{-(1/2)+iq'}(\eta)d\eta = \frac{Z^m_q}{q\tanh\pi q}\delta(q-q'), \tag{6}$$

will be useful in Sec. II B. Finally, a superposition in q generates for each azimuthal mode m

$$f_m(\eta)g_m(\mu) = \int_0^\infty P^m_{-(1/2)+iq}(\eta)U^m_q(\mu)dq, \tag{7}$$

where

$$U^m_q(\mu) = A_m(q)P^m_{-(1/2)+iq}(\mu) + B_m(q)P^m_{-(1/2)+iq}(-\mu) \tag{8}$$

and where the functions $A_m(q)$ and $B_m(q)$ are to be determined by the boundary conditions.

From this point on in our quasistatic model, we use the Fourier transform of the electric scalar potential $\mathcal{F}\Phi(\overline{r},t)\to\Phi(\overline{r},\omega)$ and note that the fields $\overline{E}$ and $\overline{D}$ will then be connected due to the local approximation by $\overline{D}(\overline{r},\omega)=\epsilon(\omega)\overline{E}(\overline{r},\omega)$ at angular frequency ω. Since Φ and $\overline{D}$ adhere to the standard quasistatic Dirichlet-Neumann boundary conditions at regions where ϵ makes a jump, it is necessary to invoke a transformation between the solutions in the planar regions and the hyperboloidal regions (see Fig. 1). Setting $H_m(\varphi-\varphi_\kappa)=(2-\delta^0_m)\cos m(\varphi-\varphi_\kappa)$, this is provided by the following expansion[43,44,59] specialized for $\mu=0$:

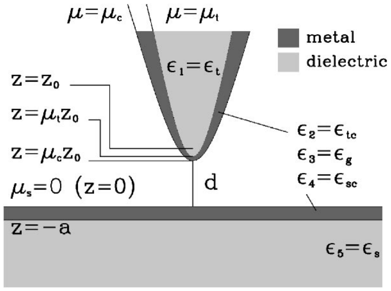

FIG. 1. Geometric representation of a metal-coated dielectric probe above a metal-coated dielectric substrate in spheroidal system in the $\varphi=0,\pi$ planes, where φ is the azimuthal coordinate. The probe tip boundary is defined by $\mu_t=\cos\theta_t$, where the angle θ is measured from the symmetry axis of the hyperboloid (z-axis) to an asymptote to the hyperboloid. The surface of the coating is given by μ_c. The boundary of the substrate metal coating ($z=0$ plane) is set by the hyperboloid $\mu_s=\cos\theta_s$ with $\theta_s=\pi/2$, while that of the substrate is defined by $z=-a$. The dielectric functions characterizing the involved materials in the five regions are labeled by ϵ_1 through ϵ_5 defined in the figure.

$$e^{i\overline{\kappa}\cdot\overline{R}} = \sum_{m=0}^\infty H_m(\varphi-\varphi_\kappa) \times\int_0^\infty T^m_q(\kappa z_0)P^m_{-(1/2)+iq}(0)P^m_{-(1/2)+iq}(\eta)dq, \tag{9}$$

where for $\kappa>0$, and $\overline{R}$ in xy plane

$$\overline{\kappa}\cdot\overline{R} = \kappa z_0\sqrt{\eta^2-1}\cos(\varphi-\varphi_\kappa), \tag{10}$$

$$T^m_q(\kappa z_0) = i^m\sqrt{\frac{2}{\pi\kappa z_0}\frac{q\tanh\pi q}{Z^m_q}}K_{iq}(\kappa z_0), \tag{11}$$

and $K_{iq}(\kappa z_0)$ is the Macdonald's function.[49]

The computation of the conical functions $P^m_{-(1/2)+iq}(\pm\cos\theta)$ for $m=0,1$ ($m\geqslant 2$ are obtained from appropriate recursion relations using $m=0,1$ functions) and $-1<\mu<1$ can be performed using its integral representation.[50] Through a proper variable substitution[60] the infinite upper limit of integration in the integral representation can be transformed to a finite closed interval of $[0,(\pi/2)]$. Here, for q not too large, the integral was evaluated effectively using a five-point Newton-Cotes integration method.[61] For large q the conical functions were expanded in terms of powers of q^{-1} and $I_n(\theta q)$ Bessel functions.[55,56] The values generated here pass the Wronskian check and are in agreement with those of Kölbig,[60] and Zhurina *et al.*[62,63]

B. Metal-coated dielectric probe above a metal-coated dielectric substrate

Figure 1 depicts the projection onto the $\varphi=0,\pi$ planes of the modeling surfaces for the metal-coated tip above a metal-coated substrate configuration. The coating boundary, specified by $\mu = \cos\theta_c = \mu_c$, is confocal with the tip surface defined by $\mu = \mu_t > \mu_c$. The $\mu = 0$ (xy plane) separates the substrate coating, which extends to $z = -a$, from the free space above it. The distance between the apex of the coating hyperboloid and the $\mu = 0$ surface is $z = d = z_0\mu_c$ and between the tip and the coating is $z_{t-c} = z_0(\mu_t - \mu_c)$. Any variations in the shape of the tip or the coating will inherently be accompanied by a translation along the z axis of the corresponding hyperboloid within the distance $0 \leqslant z \leqslant z_0$.

In Fig. 1, we will use gold or silver for the metallic regions and quartz for the dielectric regions because these compose the most commonly used material in the context of this work. We characterize the system with the following dielectric functions for each of the five regions defined in Fig. 1: $\epsilon_1 = \epsilon_t$ for the probe, $\epsilon_2 = \epsilon_{tc}$ for the frequency ω-dependent probe metal coating, $\epsilon_3 = \epsilon_g = 1.0$ for the gap region, $\epsilon_4 = \epsilon_{sc}$ for the substrate metal coating, and $\epsilon_5 = \epsilon_s$ for the substrate. The imaginary part and the frequency dependency of the dielectric functions of the tip and the substrate media have been neglected due to a small variation of these quantities in the visible spectrum as is evident from the optical data.[64] With these notations, the general solution to the Poisson equation will then be composed of the partial potentials Φ_i, where $i = 1, 2, \ldots, 5$ denotes the five regions of Fig. 1, respectively. Using (3) and noting that the conical functions of negative arguments are singular at $\theta = 0$, the participant partial potentials Φ_i are written for $i = 1, 2, 3$ as

$$\Phi_i(\overline{r}) = \sum_{m=0}^{\infty} (2 - \delta_m^0) \cos m(\varphi - \varphi_\kappa) \times \int_0^\infty A_m(q) T_q^m(\kappa z_0) P^m_{-(1/2)+iq}(\eta) f_i^m(\mu, q)\, dq. \tag{12}$$

In order to satisfy the boundary conditions, that is, satisfying the continuity of the potential and the normal component of the displacement field, we utilize the orthogonality of the azimuthal functions H_m and relation (6) and write for the potential at μ_t

$$\int_1^\infty \left[\int_0^{2\pi} (\Phi_1\,(\overline{r})|_{\theta_t}) H_{m'}\, d\varphi \right] P^m_{-(1/2)+iq'}(\eta)\, d\eta = \int_1^\infty \left[\int_0^{2\pi} (\Phi_2\,(\overline{r})|_{\theta_t}) H_{m'}\, d\varphi \right] P^m_{-(1/2)+iq'}(\eta)\, d\eta, \tag{13}$$

where the inner integral eliminates the m summation, and changing the order of integration between η and q integrals, the outer integral eliminates the q integration by isolating the integrands at q'. Rewriting Eq. (13) for θ_c and carrying out the same procedure for the displacement field at θ_t and θ_c, we obtain for $i = 1, 2, 3$ the following:

$$f_1^m(\mu, q) = \beta_q^m(\mu_t) P^m_{-(1/2)+iq}(\mu),$$

$$f_2^m(\mu, q) = P^m_{-(1/2)+iq}(\mu) - \alpha_q^m(\mu_t) P^m_{-(1/2)+iq}(-\mu),$$

$$f_3^m(\mu, q) = \Lambda_m(q) P^m_{-(1/2)+iq}(\mu) + \overline{\Lambda}_m(q) P^m_{-(1/2)+iq}(-\mu), \tag{14}$$

where $\alpha_q^m(\mu_t)$, $\beta_q^m(\mu_t)$, $\Lambda_m(q)$, and $\overline{\Lambda}_m(q)$ are all functions of material properties and, thus, frequency ω, and are defined as

$$\alpha_q^m(\mu_t) = \left(\frac{\epsilon_{tc} - \epsilon_t}{\epsilon_{tc}\varepsilon_q^m(\mu_t) - \epsilon_t} \right) K_q^m(\mu_t),$$

$$\beta_q^m(\mu_t) = \frac{\epsilon_{tc} - \epsilon_{tc}\varepsilon_q^m(\mu_t)}{\epsilon_t - \epsilon_{tc}\varepsilon_q^m(\mu_t)},$$

$$\Lambda_m(q) = 1 + \left(\frac{\epsilon_{tc} - 1}{1 - \varepsilon_q^m(\mu_c)} \right) \left[1 - \frac{\alpha_q^m(\mu_t)}{\hat{K}_q^m(\mu_c)} \right],$$

$$\overline{\Lambda}_m(q) = (\hat{K}_q^m(\mu_c) - \alpha_q^m(\mu_t)) \left[\frac{1 - \epsilon_{tc}\varepsilon_q^m(\mu_c)}{1 - \varepsilon_q^m(\mu_c)} \right] - \hat{K}_q^m(\mu_c), \tag{15}$$

where we have defined

$$K_q^m(\mu) = \frac{P^m_{-(1/2)+iq}(\mu)}{P^m_{-(1/2)+iq}(-\mu)}, \quad \hat{K}_q^m(\mu) = \frac{\partial_\mu P^m_{-(1/2)+iq}(\mu)}{\partial_\mu P^m_{-(1/2)+iq}(-\mu)},$$

$$\epsilon_q^m(\mu) = \frac{K_q^m(\mu)}{\hat{K}_q^m(\mu)}, \tag{16}$$

where ∂_μ stands for partial differentiation of the conical functions with respect to their argument. The Fourier frequency ω dependencies of the functions above have been left out for clarity. The special values and the asymptotic forms of the relations in (16), which will be useful in the further work, are given in Appendix A [Eqs. (A1)–(A4)].

For lower half space $z < 0$, we use the following Cartesian ansatz:

$$\Psi(\overline{r}) = e^{\pm\kappa z} e^{i\overline{\kappa}\cdot\overline{R}}, \quad \kappa > 0, \tag{17}$$

which, when incorporating the boundary conditions for the $z = -a$, takes the following forms for $i = 4, 5$ (i.e., in the regions $-a < z < 0$ and $z < -a$):

$$\Phi_4(\overline{r}) = \Upsilon(\kappa)[e^{\kappa z} + \gamma e^{-2\kappa a} e^{-\kappa z}] e^{i\overline{\kappa}\cdot\overline{R}},$$

$$\Phi_5(\overline{r}) = \Upsilon(\kappa) \overline{\gamma} e^{\kappa z} e^{i\overline{\kappa}\cdot\overline{R}}, \tag{18}$$

with γ and $\overline{\gamma}$ defined as

$$\gamma = \frac{\epsilon_{sc} - \epsilon_s}{\epsilon_{sc} + \epsilon_s}, \quad \overline{\gamma} = \frac{2\epsilon_{sc}}{\epsilon_{sc} + \epsilon_s}, \tag{19}$$

and $\Upsilon(\kappa)$ being a common amplitude for $z < 0$. The continuity of the potential and the normal component of the displacement field at the $\mu = 0$ interface requires using Eqs. (9) and (17), and the following observations:

$$\overline{e_\mu}\cdot\overline{\nabla}\Psi|_{\mu=0} = \overline{e_z}\cdot\overline{\nabla}\Psi|_{z=0},$$

$$-\kappa e^{i\kappa z_0\sqrt{\eta^2-1}\cos(\varphi-\varphi_\kappa)} = \frac{1}{z_0\eta}\sum_{m=0}^{\infty} H_m(\varphi-\varphi_\kappa) \times\int_0^\infty T_q^m(\kappa z_0)P^m_{-(1/2)+iq}(\eta) \times\partial_\mu P^m_{-(1/2)+iq}(\mu)|_{\mu=0^+}dq, \qquad (20)$$

$$\Phi_4(\overline{r})|_{\mu=0^-} = \Upsilon(\kappa)[1+\gamma e^{-2\kappa a}]e^{i\overline{\kappa}\cdot\overline{R}} = \sum_{m=0}^{\infty} H_m(\varphi-\varphi_\kappa) \times\int_0^\infty T_q^m(\kappa z_0)\Upsilon(\kappa)[1+\gamma e^{-2\kappa a}] \times P^m_{-(1/2)+iq}(0)P^m_{-(1/2)+iq}(\eta)dq,$$

$$\partial_\mu\Phi_4(\overline{r})|_{\mu=0^-} = \sum_{m=0}^{\infty} H_m(\varphi-\varphi_\kappa) \times\int_0^\infty T_q^m(\kappa z_0)\Upsilon(\kappa)\,[\gamma e^{-2\kappa a}-1] \times P^m_{-(1/2)+iq}(\eta)\partial_\mu P^m_{-(1/2)+iq}(\mu)|_{\mu=0^-}dq. \qquad (21)$$

From now on, we only consider the case where $\epsilon_{sc}(\omega) = \epsilon_{tc}(\omega) = \epsilon(\omega)$. Equating the above equations to their counterparts for $\mu \to 0^+$, expressing all the exponentials in terms of hyperbolic cotangent and simplifying, we arrive at

$$\frac{-\epsilon}{\lambda_q^m(\mu_c)}\left(\frac{\epsilon+\epsilon_s\coth\kappa a}{\epsilon_s+\epsilon\coth\kappa a}\right) = \frac{\alpha_q^m(\mu_t)-K_q^m(\mu_c)+\epsilon\zeta_q^m(\mu_c)[\hat{K}_q^m(\mu_c)-\alpha_q^m(\mu_t)]}{\alpha_q^m(\mu_t)-K_q^m(\mu_c)+\epsilon\overline{\zeta}_q^m(\mu_c)[\hat{K}_q^m(\mu_c)-\alpha_q^m(\mu_t)]}, \qquad (22)$$

where we have set

$$\lambda_q^m(\mu_c) = \frac{1+\hat{K}_q^m(\mu_c)}{1-\hat{K}_q^m(\mu_c)}, \quad \zeta_q^m(\mu_c) = \frac{1+K_q^m(\mu_c)}{1+\hat{K}_q^m(\mu_c)},$$

$$\overline{\zeta}_q^m(\mu_c) = \frac{1-K_q^m(\mu_c)}{1-\hat{K}_q^m(\mu_c)}. \qquad (23)$$

For each m, solving Eq. (22) for ϵ results in the following polynomial:

$$\sum_{i=0}^{4} c_i^m(q)\epsilon^i(\omega,q) = 0, \qquad (24)$$

with the coefficients $c_i^m(q)$ given by Eq. (B1) in Appendix B. This result can now be studied numerically to simulate the dispersion relations, that is, the roots of (24), which, in view of Drude's dielectric function, will describe the frequency (ω) dependence of each mode (m,q). We thus note that, taking κ as a parameter, each (m,q) singles out a particular solution of the system resulting in a particular potential $\Phi_q^m(\overline{r})$ and field $-\nabla\Phi_q^m(\overline{r})$ distribution in the space (η,μ,φ).

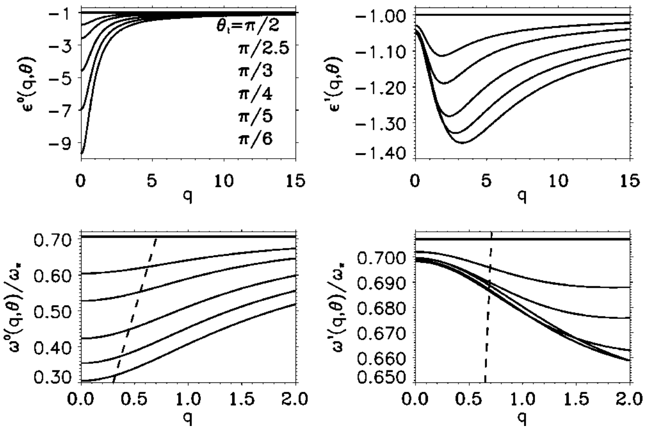

FIG. 2. Surface modes of an isolated hyperboloid in vacuum as a function of curvature. The top two graphs show the $m=0,1$ resonance modes, and the bottom two are the corresponding Drude metal limit responses. The modes (solid curves) in each graph, in the order of increasing curvature from top to bottom, show the departure from a Cartesian interface at $\theta_t=\pi/2$. The dashed curve represents the light dispersion relation. The energies have been expressed with reference to the bulk plasmon energy ω_p.

III. RESULTS AND DISCUSSIONS

A. Surface modes of a probe

We begin our discussion by studying the resonance modes of an isolated solid hyperboloid of a local dielectric function $\epsilon(\omega)$ in vacuum. With the definitions in (16), these are given by the functions $\epsilon_q^m(\omega,\mu_t)$, $m=0,1,2,\ldots$, which yield the nonretarded surface plasmon dispersion relations for a hyperboloid at $\mu=\mu_t$, and are shown in Figs. 2 and 3. Employing the Drude model, the modes have also been displayed with reference to bulk plasmon frequency ω_p. For all other purposes in this work, a plasma frequency[65] of $\omega_p=ck_p=8.33\times10^{15}$ Hz for gold and 10.99×10^{15} Hz for silver (corresponding to Re $\epsilon=0$ in each case) will be used.[64] In the limit

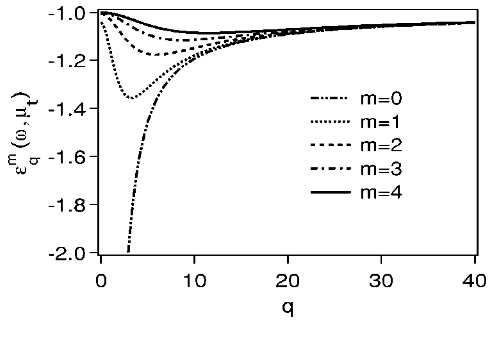

FIG. 3. The various azimuthal modes m of a probe with $\theta_t=30°$. As shown, in the limit $m\to\infty$, the modes approach the surface plasmon dispersion of a vacuum-bounded metal half space for all q. All modes reach their asymptotic values for $q\gtrsim20$.

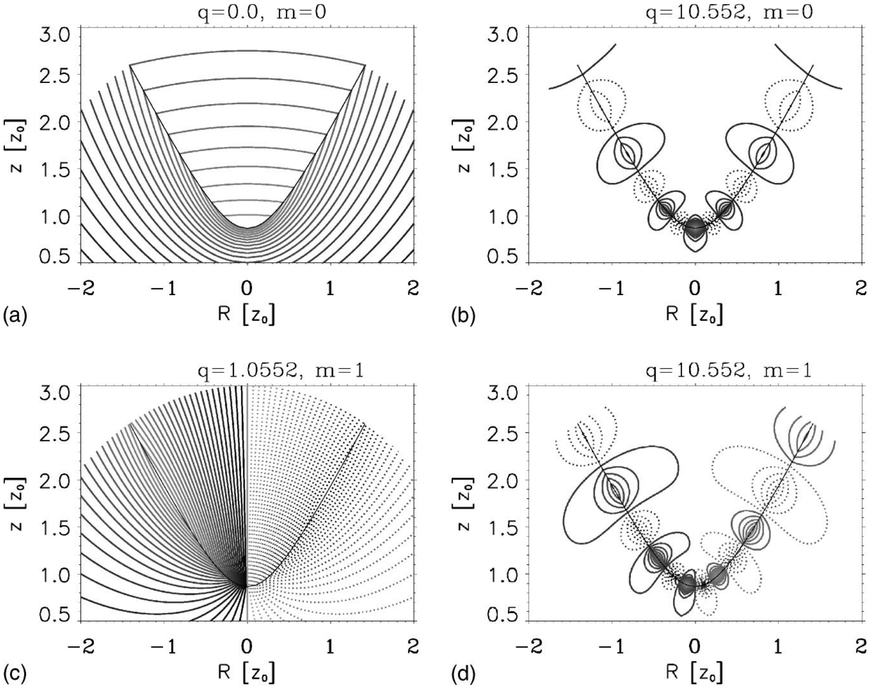

FIG. 4. The projection onto the $\varphi=0,\pi$ planes of the relative potential distributions of a probe with $\theta_t=30°$. The various symmetries presented by the pair (m,q) are shown by the equipotential surfaces, where the dotted contours display $\Phi_q^m(\overline{r})<0$, while $\Phi_q^m(\overline{r})>0$ is represented by the solid contours. In (b) and (d) the effect of the azimuthal order on the charge distributions is given for the same eigenvalue q, while (c) and (d) show the effect as a function of q for the same order. The particular values of $q=1.0552, 10.552$ were extracted from the dispersion of the $m=1$ mode at $\epsilon=-1.17$ in Fig. 3. The simulated domain is defined by $\eta\in[1,3]$, and $\mu\in[0,\pi/2]$.

$\theta_t\rightarrow\pi/2$ $(\mu_t\rightarrow 0)$, we have $\epsilon_q^m(\omega,\mu_t)\rightarrow -1$, that is, the nonretarded dispersion relation of a simple Cartesian metal-vacuum interface. This limit is also approached by large m values, as seen in Fig. 3. The large q form of these functions (see Appendix A),

$$\epsilon_q^m(\omega,\mu_t)\underset{q\gg 1}{\sim} -1-\frac{\cot\theta_t}{q}, \tag{25}$$

also yields, in the limit $q\rightarrow\infty$, the Cartesian metal-vacuum result $\epsilon_q^m(\omega,\mu_t)\rightarrow -1$.

As a comparison, we first note that it can be seen from the retarded metal-vacuum Cartesian interface modes

$$\epsilon(\omega)=-\left(\frac{1-l\epsilon(\omega)}{1-l}\right)^{1/2}, \tag{26}$$

where $\sqrt{l}=\omega/ck$ measures the retardation strength, so that $l=1$ yields the photon dispersion in vacuum, that the nonretarded mode $\epsilon=-1$ $(l=0)$ is pushed down below the photon dispersion relation and tangential to it in the small momentum limit as a result of the retardation. For a Drude metal of resonance frequency ω_p, in the small momentum region $k\ll k_p$, it can be shown from (26) that $\omega/\omega_p\approx k/k_p\approx q$, and thus we expect that the inclusion of retardation will pull all the modes (m,q) below the light line. However, retardation has no effect in the large momentum region as Eq. (26) reaches its asymptotic value of the surface plasmon frequency $\omega_p/\sqrt{2}$ for $k\approx 2k_p$. It can also be seen from Fig. 2, that for $\theta_t\rightarrow\pi/2$, we encounter a degeneracy in m as a result of loss of curvature. The higher the curvature, the closer to zero the modes start; that is, $\omega^0(q=0,\theta_t)\rightarrow 0$ when $\theta_t\rightarrow 0$. Thus, the sharper the tip, the larger the variation in the m modes. It is interesting to note that, in the case of a Drude metal spheroidal particle,[12,66] the energies of the lowest eigenmodes start close to 0 and increase to reach their asymptotic values, while all the higher modes start at higher energies below the surface plasmon energy and decrease to reach their asymptotic values. For a spherical metal particle[21] (a special case of a spheroid), the lowest mode is at $\omega=0$. In the case of an isolated metal cylinder in vacuum,[21] having an identical azimuthal symmetry as in our hyperboloidal case, the $m=0$ mode starts at $\omega=0$, while all the higher start at the surface plasmon energy $(\omega/\omega_p=1/\sqrt{2}=0.71)$, in close similarity to the trend here as shown in Fig. 2. The m degeneracy is also observed in the high momentum region $(q\rightarrow\infty)$. At such small scales, the collective oscillations cannot sense the geometrical variations. From the well-like appearance of the $m\geqslant 1$ modes in Figs. 2 and 3, each allowing two excitations at the same energy, it can be seen that the wells get wider, the higher the curvature, but that the minima of the wells reach the limit $\omega/\omega_p=0.64$. For the same m, the q distributes the charges on the probe, such that low q values result in more uniform distributions. This is illustrated by the simulations of the potential distributions of a $\theta_t=30°$ probe in Fig. 4, which also provides a physical interpretation of the eigenvalues q. Figures 4(a) and 4(b) show the projection onto the $\varphi=0,\pi$ planes of the equipotential surfaces for $(m,q)=(0,0.0)$, and $(m,q)=(0,10.552)$, while Figs. 4(c) and 4(d) show the differences for the two q values, corresponding to the same $\epsilon=-1.17$ for the $m=1$ mode shown in Fig. 3. Figure 4, thus, shows explicitly the different symmetries dictated by the modes (m,q), where the eigenvalues q appear to play the role of the surface plasmon wave vectors along the surface of the hyperboloid. This point will be rehashed in Sec. III B [Eq. (33)] in the context of surface plasmon propagation in a Cartesian thin foil. Experimentally, the relative excitation probabilities of these modes will, therefore, depend on the polarization state of the incident field.

We also note that, although the solutions $\epsilon_q^m(\cos\theta_t)$ are formally valid anywhere in the system, the interpretation of them physically, as the true surface modes of the metal-vacuum boundary, is more precise the closer we get to the apex region as a result of our quasistatic assumption. We are only interested in the apex region, where setting $R=(x^2+y^2)^{1/2}$, the curvature of the hyperboloid

$$d_R z(R) = R z^{-1}(R) \cot^2 \theta_t, \tag{27}$$

changes appreciably. Thus, for $\eta \gg 1$, and when $z_0 \sin \theta_t$ is fixed we get $d_R z(R) \rightarrow \cot \theta_t$ (i.e., a constant), and thus the hyperboloid behaves as a cone in this limit. To estimate when the retardation becomes significant, we calculate the radius of curvature of the probe apex by fitting a sphere to it. For a focal point of $z_0=10.0$ nm and a probe angle of $\theta_t=\pi/6$ in a medium $\epsilon=\epsilon_e$, we get for the radius of the sphere $r=7.5$ nm. It can be shown[67] that, as long as $\lambda > 2\pi r\sqrt{\epsilon_e}$, we can neglect retardation. This is clearly satisfied for our hyperboloidal probe surrounded by vacuum ($\epsilon_e=1$).

Also noteworthy is that, the modes (16) adhere to the sum rules for the surface modes of the complementarily divided spaces as formulated by Apell *et al.*[68] In the case of an isolated solid hyperboloid (with frequencies ω_h), the complementary space is a hyperboloidal void (with frequencies ω_v), and thus the sum rule automatically generates the surface modes of the void (such as the modes of a metal nanohole, for which experimental observation of curvature-dependent transmission, has been reported).[69] Thus, for a Drude metal, if Eq. (16) has the right symmetry, the transformation $\mu_t \rightarrow -\mu_t$ should yield the surface plasmon frequencies of the void from $\omega_v^2=\omega_p^2-\omega_h^2$, which can easily be confirmed from (16) because $\epsilon(\omega_h)\epsilon(\omega_v)=1$. Finally, for the particular case of the modes of an isolated hyperboloid, further comparisons can be made, for finite curvatures, to the case of an isolated solid paraboloid of revolution, and in the limit $\mu_t \rightarrow 1$, to the case of an isolated solid cone, for which the solutions to the Laplace equation are known.[6,22]

B. Surface modes of a complex probe

By resorting to the fully retarded Cartesian cases, we extend the above considerations to the multilayer systems in the hyperboloidal cases. In particular, as a limiting case to the system in Fig. 1, we extend the simple metal-vacuum Cartesian interface analogy to the multilayer system depicted in Fig. 5. In doing so, we generate for the *p*-polarized photons, using a matrix formalism,[70,71] the retarded surface plasmon dispersion relations for the system in Fig. 5, by (conveniently) solving for the metal separation distance d using Eqs. (C1)–(C3). We note that Eq. (C1) is transcendental due to inclusion of retardation, and, though it may be rewritten differently, it can only be reduced to polynomial form when retardation is neglected. The propagation length of the surface plasmons is limited by damping in the metal, which is ignored in the free-electron model. In what follows, we will also use the real part of the complex dielectric functions for gold and silver, obtained by interpolation in the reported[64] experimental data, heretofore referred to as the experimental dielectric functions.

In analogy with the splitting of the degenerate thick Cartesian film dispersion relation, into symmetric and antisymmetric modes, as a result of a reduction of the film thickness, we expect in the isolated curved metal foil case, i.e., with $0 < \theta_t < \theta_c$, that the modes in Fig. 2 multiply. Similarly, we expect that in the limit $\theta_t \rightarrow \theta_c$, the dispersion relations enter the two-dimensional (2D) plasmon[73] (sheet plasmon) behavior. In the absence of the $z>0$ structures in both Figs. 1 and 5, we are left with the Kretschmann[74] configuration. Then, Eq. (C1), in the limit of $\epsilon_t=\epsilon_{tc} \rightarrow 1$, generates the retarded and nonretarded ($c \rightarrow \infty$) modes shown in Fig. 6(a) for an undamped Drude metal. The decoupling of the two modes and their degeneration to surface plasmon energy in the nonretarded case, and to the retarded dispersion of a single metal interface are seen from the gray scale.

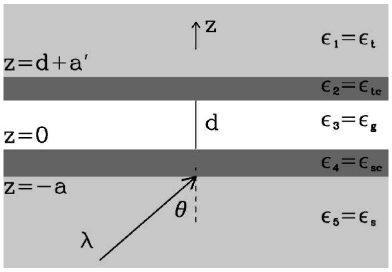

FIG. 5. A Cartesian multilayered system in the z direction. This configuration is composed of a semi-infinite dielectric medium (ϵ_1), interfaced with a $a'=35$ nm thin gold film (ϵ_2), and another semi-infinite dielectric medium (ϵ_5), interfaced with a $a=45$ nm thin metal film (ϵ_4) separated by a free space (ϵ_3) gap (d) from the first one. This system can be considered as the limiting case $\theta_t < \theta_c \rightarrow \pi/2$ to the system in Fig. 1. The system is stimulated by an optical field of momentum $k=2\pi/\lambda$ incident at angle θ.

The symmetric and antisymmetric modes, shown in Fig. 6(a), will each split into two (close-laying modes) if we bring a metal-coated dielectric medium from above, as shown in Fig. 5. This is demonstrated for a Drude metal in Fig. 6(b) for the nonretarded case and in Fig. 6(c) for the retarded case, where the modes are again pushed down below the light line in the small momentum region. Excluding the virtual modes for the dispersion relation of the coupled system in Fig. 5, there are four branches describing the possible retarded modes of resonance. These are grouped into two categories, one above the reduced bulk plasmon frequency $\omega_p/\sqrt{2}$ and one below it. Optical access to these modes, in the arrangement shown in Fig. 5, is governed by the intersection of the light dispersion line with these modes. This restricts the number of accessible modes for a particular wavelength, propagation angle of the incident photon field, and the selected film thicknesses.

We now continue by analyzing the possible eigenmodes of the configuration depicted in Fig. 1. We first note that, setting

$$A_i^m(q) = \frac{c_i^m(q)}{c_4^m(q)}, \quad i=0,1,2,3,4,$$

the strength of a coefficient $c_i^m(q)$, in Eq. (24) describes the relative energy of the modes at the interface that corresponds to that coefficient's degree, for $i=1,2,3,4$ labeling the interfaces from top to bottom. These coefficients are smooth functions of q and are shown in Fig. 7. For $q \in [q_{min}, q_{max}]$

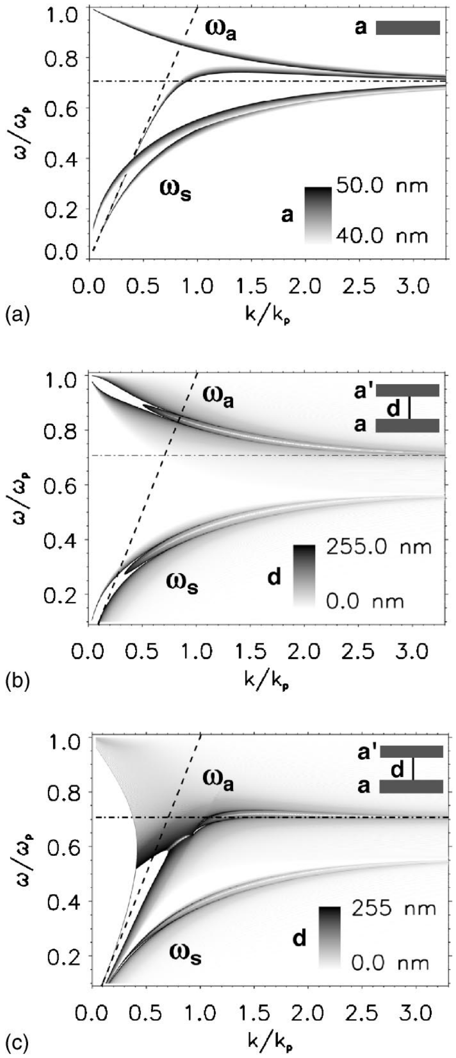

FIG. 6. Retarded and nonretarded dispersion relations corresponding to symmetric (ω_s) and antisymmetric (ω_a) surface modes of a Drude metal. (a) For the two surfaces of a thin gold film (sketched in the inset), the two nonretarded modes (extending to the left of the light line) are clearly pushed down all the way below the light line (dashed line) as a consequence of inclusion of retardation. The dashed-dotted line represents the surface plasmon frequency $\omega_p/\sqrt{2}$. The gray scale represents film thicknesses in the range $a \in [40.0, 50.0]$ nm. For the arrangement of Fig. 5 with $a=45$ nm and $a'=35$ nm in Eq. (C1), the nonretarded dispersion relations in (b) are similarly pushed down due to retardation as shown in (c). The gray scale represents the air gap interval: $d \in [0, 255]$ nm.

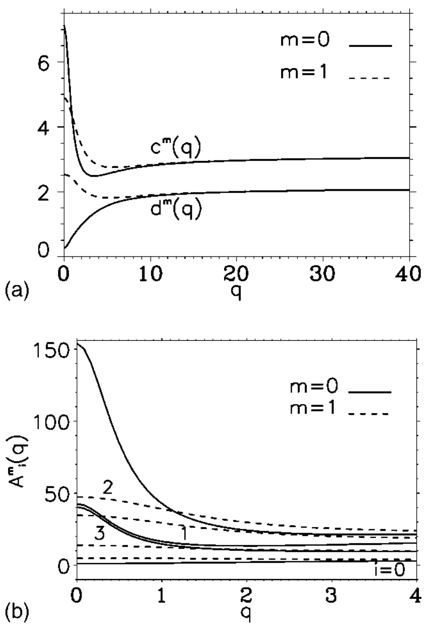

FIG. 7. (a) Coefficients $c^m(q)$ and $d^m(q)$ of the dispersion function [Eq. (30)] for $m=0,1$ for an isolated hyperboloidal foil. Little or no variation is observed for $q>10$. (b) Coefficients of the polynomial [Eq. (24)] describing the relative magnitudes of the resonant values of ϵ corresponding to $m=0,1$ for the system shown in Fig. 1. There is little or no variation in these coefficients for essentially $q>2$.

and $q_{min} \geqslant 0$, Eq. (24) was solved numerically using Laguerre's method.[61] Thus, for this q interval, we solve Eq. (24) for $m=0,1$, which gives the roots $\epsilon_r^m(q)$, $r=1,2,3,4$ such that

$$\epsilon_r^m(q)^* = \epsilon_r^m(q) \leqslant 0, \quad \forall\, q,m,r. \tag{28}$$

In all the numerical evaluations of these roots, we have assumed that κ, in Eq. (B1), takes on the value of the wave vector of the surface plasmons excited on the coating of the substrate without the presence of the coated tip

$$\coth \kappa a = \coth \frac{2\pi a n_s \sin\theta}{\lambda}, \tag{29}$$

with $\lambda=632.8$ nm, $n_s=\sqrt{\epsilon_s}$, $\theta=46°$, and $a=45$ nm. This would then correspond to a realistic polarization charge separation in the substrate medium. Based on experimental observation we set $z_0=100$ nm, allowing a coating thickness of $z_{t-c}=30$ nm for $\theta_t=0.45$ and $\theta_t=0.93$, which, in turn, gives a gap size of $d=59.8$ nm. Equations (24) and (30) are independent of z_0; the only distance dependency is due to the particular choice of μ_t and μ_c.

Before discussing the general case of Fig. 1, we consider the important limiting case of an isolated hyperboloidal foil in vacuum and its Cartesian counterpart of an isolated planar foil in vacuum. The former can be achieved from Eqs. (24) and (B1) after some algebra in the limit $a \to 0$ and $\epsilon_s \to 1$, which reduces (24) to

$$\epsilon^2 + c^m(q)\epsilon + d^m(q) = 0, \tag{30}$$

with the coefficients given by

$$c^m(q) = \frac{[2\hat{K}_q^m(\mu_t) - K_q^m(\mu_c)]\varepsilon_q^m(\mu_t) - \hat{K}_q^m(\mu_c)}{[\hat{K}_q^m(\mu_c) - \hat{K}_q^m(\mu_t)]\varepsilon_q^m(\mu_t)},$$

$$d^m(q) = \frac{K_q^m(\mu_c) - \hat{K}_q^m(\mu_t)\varepsilon_q^m(\mu_t)}{[\hat{K}_q^m(\mu_c) - \hat{K}_q^m(\mu_t)]\varepsilon_q^m(\mu_t)},$$

and shown in Fig. 7. Now specializing Eqs. (A1)–(A3) for $m=0$ in the above equations, we get

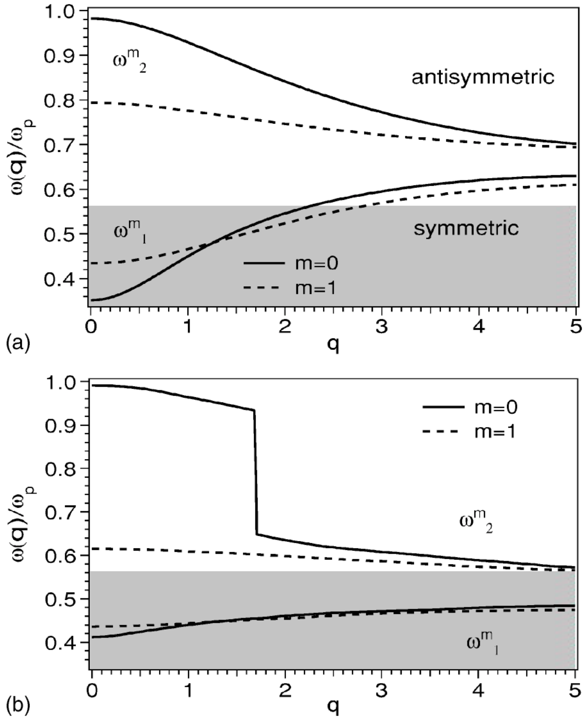

FIG. 8. Nonretarded surface plasmon resonance values for the symmetric and antisymmetric modes for orders $m=0,1$, assuming (a) a Drude model and (b) the experimental dielectric function of gold for the metal-coated probe above a dielectric substrate configuration. The higher energy modes ω_2^m correspond to the μ_c interface, whereas ω_1^m represent the modes of μ_t interface. The horizontal gray band is the visible band corresponding to the spectral range $[400,700]$ nm. Retardation effects are expected, in analogy with the Cartesian case, to pull the small q region of these spectra below the light line in view of Eq. (33).

$$c^0(q) \underset{q\gg1}{\sim} 2\frac{e^{-q(\pi-2\theta_c)}+e^{-q(\pi-2\theta_t)}}{e^{-q(\pi-2\theta_c)}-e^{-q(\pi-2\theta_t)}},$$

$$d^0(q) \underset{q\gg1}{\sim} 1,$$

and rearranging puts Eq. (30) in the following form:

$$\epsilon^2 + 2\coth[q(\theta_c-\theta_t)]\epsilon + 1 = 0. \qquad (31)$$

Identifying this dispersion equation with the corresponding equation for the planar case derived from (C1),

$$\epsilon^2 + 2\coth(ka)\epsilon + 1 = 0 \qquad (32)$$

yields the equivalence between q and the surface plasmon momentum k

$$q(\theta_c-\theta_t) \sim ka. \qquad (33)$$

With this interpretation of q, the two modes of a metal-coated dielectric probe over a dielectric substrate are shown in Fig. 8. Here, symmetric and antisymmetric modes comprise the relative distributions of electrons on the two hyperboloidal bounding surfaces of the metal coating. The frequency dependence $\omega(q)$ of the dispersion relations [satisfying Eq. (24)] was obtained by matching them to the experimental dielectric functions ϵ. This can be accomplished by searching the frequencies at which there is a match in the dielectric functions or, more efficiently, by writing $\omega=\omega(\epsilon)$ and interpolating in ϵ at locations presented by the solutions to Eq. (24).

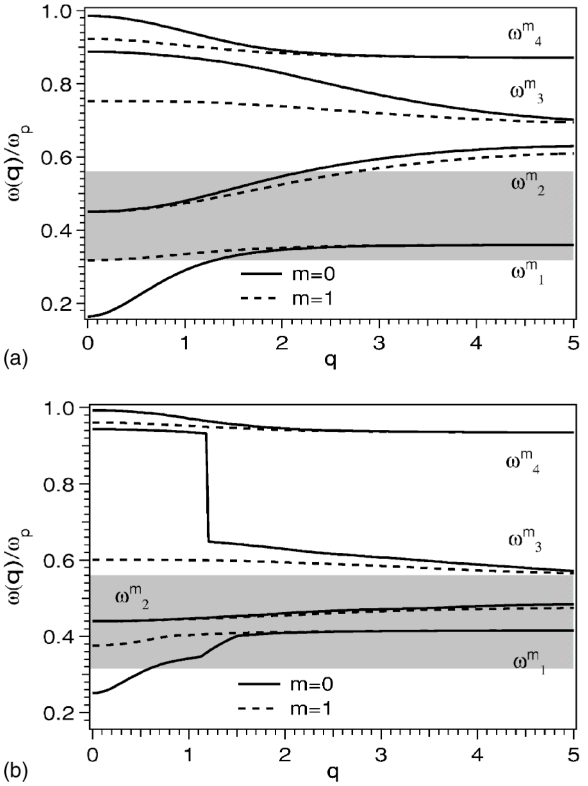

FIG. 9. The four branches ω_i^m, $i=1,2,3,4$ representing the nonretarded surface plasmon resonance values for the modes $m=0,1$, assuming (a) a Drude model and (b) the experimental dielectric function of gold for the metal-coated probe above a metal-coated dielectric substrate configuration shown in Fig. 1. The appearance of the two additional modes $\omega_{1,4}^m$, compared to Fig. 8, is a result of the presence of the coated substrate. Simulations were performed for substrate thickness $a=45$ nm, with tip and coating boundaries set to $\theta_t=0.45$ and $\theta_c=0.93$, respectively. The horizontal gray band is the visible band, and the reference energy is $\omega_p=5.47$ eV.

The results of Fig. 8 show that, although the overall redshift of all modes in the experimental dielectric function case [Fig. 8(b)] is clear, in the small momentum region $q<1$, the $m=0$ modes are slightly blueshifted in comparison to the Drude metal case of Fig. 8(a). Despite the abrupt change in the ω_2^0 mode, caused by the nonuniform distribution of the experimental dielectric values over the frequency range encountered, the overall structure of the modes is preserved. The discontinuous appearance of the ω_2^0 mode can be readily smoothed out by an averaging algorithm such as the boxcar technique.

Finally, the dispersion relations for the system in Fig. 1 are displayed in Figs. 9(a) and 10(a) for a Drude metal, and in Figs. 9(b) and 10(b) for the experimental dielectric function for gold and silver, respectively. As in the Cartesian cases of Fig. 6, there are four branches ω_i, $i=1,2,3,4$ corresponding to the four metal interfaces, two Cartesian and

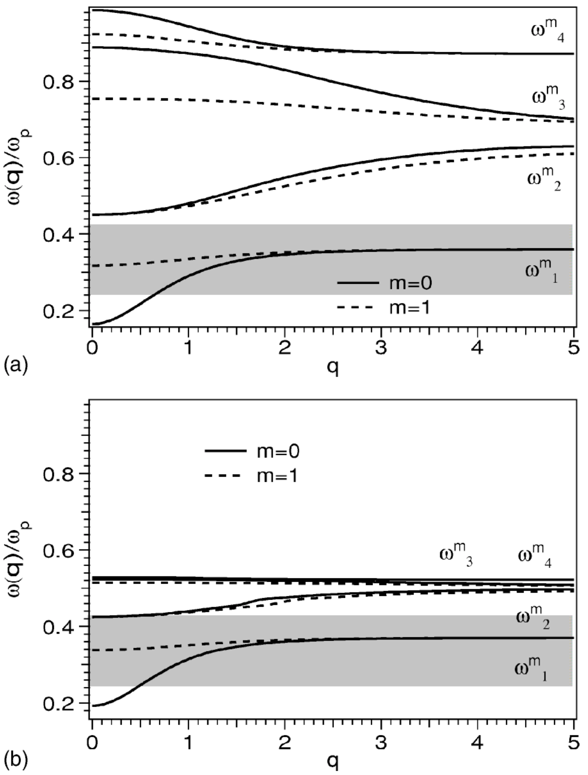

FIG. 10. Dispersion of surface plasmons in the system of Fig. 1 for (a) a Drude metal and (b) experimental dielectric function of silver. A large redshift of the higher energy modes is observed in the case of the experimental dielectric function of silver as compared to the Drude model. The reference energy is $\omega_p = 7.23$ eV.

two hyperboloidal. However, in the case of gold, the modes of the Cartesian interfaces ($\omega^m_{1,4}$) appear to be blueshifted, whereas those of the curved surfaces ($\omega^m_{2,3}$) are mostly redshifted in close similarity to the case of Fig. 8 when employing the experimental dielectric function. On the other hand, in the case of silver, the higher energy modes are severely redshifted. Furthermore, in all Figs. 8–10, a squeezing of the modes into the visible region is observed in comparison to the Drude model.

In a series of limiting considerations in the simulations of the results in Eq. (24) [such as the following cases (or a combination thereof): $\epsilon_s \to 1, \infty$; $a \to 0, \infty$; $\theta_t \to 0, \pi/2$; $\theta_c \to 0, \pi/2$; $\theta_t \to \theta_c$] we can arrive at several interesting conclusions regarding the behavior of the dispersion relations of the system (or its subsystems) shown in Fig. 1 as compared to those of the system (or its subsystems) in Fig. 5. We can identify the lowest frequency (ω^m_1) and highest frequency (ω^m_4) modes in Figs. 9 and 10 to belong to the thin Cartesian film (symmetric and antisymmetric modes, respectively), whereas ω^m_3 and ω^m_2 correspond to the two surfaces of the curved metal film (symmetric and antisymmetric modes). If we, in our simulations, let $a \to 0$ systematically, we note that $\omega^m_4 \to \omega_p$, whereas $\omega^m_1 \to 0$. The presence of the planar metal film elevates the energy of the modes of the inner surface of the probe. For $\theta_t < \theta_c \lessapprox \pi/2$, this resembles Otto's geometry.[75]

As another example, we can also simulate the effect of the involved dielectric media. All modes are redshifted as a result of an increase in the value of the dielectric functions. The depolarization effect of large substrate and probe dielectric constants ($\epsilon_s = \epsilon_t \gg 1$) are observed to have the effect of suppressing to zero the two lower frequency modes in Figs. 9 and 10, belonging to the inner curved metal surface (ω^m_2) and lower planar metal surface (ω^m_1), both in direct contact with the dielectric media. The nature of this suppression is similar to the redshift in surface plasmon energy experienced by the simple Cartesian metal-vacuum interface when the vacuum is replaced by a dielectric.[76] The two higher frequency modes belonging to the outer curved surface and upper planar surface only undergo a slight redshift in energy.

As a final limiting case, we consider the following situation: $\epsilon_s \to 1$, $a \to 0$, and $\theta_t \lessapprox \theta_c$ (i.e., a curved 2D metallic system in vacuum). In this limit, $\omega^m_4 \to \omega_p$, $\omega^m_1 \to 0$ as a result of $a \to 0$, and the normal hyperboloidal mode $\omega^m_3 \to \omega_p$, while the tangential modes ω^m_2 approach a 2D plasmon. Here the normal and tangential refer to the field distribution inside the foil and correspond to antisymmetric and symmetric polarization charge distributions, respectively. If we further let $\theta_t < \theta_c \lessapprox \pi/2$, ω^m_2 become m degenerate and approach the mode of a Cartesian 2D plasmon. The variation of such a mode with the plasmon momentum is known[6] to have a square-root dependence and is confirmed graphically in our simulations by visual inspection and, numerically, by fitting the function $(0.058249 \pm 0.000131)\sqrt{q}$ to ω^m_2.

IV. CONCLUSIONS

In summary, we have presented an exact quasistatic calculation for the dispersion relations of curved metal-dielectric multilayer structures within the framework of a local dielectric function. We have demonstrated that, by following the movements of the loci representing the resonance values of the surface modes of the multilayer system, the effect of curvature can be studied explicitly without resorting to any geometric approximations.

All the dispersion relations for the hyperboloidal cases considered in this work adhere to the fact that at higher plasmon momenta, there is little or no variation in the resonance values. In particular, for $q > 4$ fixed substrate film thickness and fixed $\theta_t - \theta_c$, all the modes converge rapidly to their asymptotic values. This would correspond, in the case of Eq. (32), to the thick foil limit where $\epsilon \to -1$ (or $\omega \to \omega_p/\sqrt{2}$). Thus, for fixed q bulk behavior enters faster with increasing coating thickness. For a typical probe coating of 30 nm and substrate coating of 45 nm, the dispersion relations presented in this work suggest the possibility of optical excitation. Given an available frequency range of interest, it is possible, invoking the approach here, to seek the appropriate physical parameters for the probe and the involved coatings, and the choice of the involved metal and dielectric media, including the gap region. Comparisons of the existence of resonance frequencies at the typical experimental visible wavelengths $\lambda = 632.8$, 515.0, and 442.0 nm incident at angles $\theta = 46.0°$, 50.0°, and 55.0° (corresponding to peak absorption) can be made from Figs. 8–10.

An experimental verification of this result would entail, in the case of SPM, that the metal-coated probe tip be placed within a few nanometers above a metal-coated substrate to record the exponentially decaying signal in the constant height mode of the operation, upon which the wavelength can be scanned while monitoring the coupling signal.

ACKNOWLEDGMENTS

This work was supported by the DOE BES. Oak Ridge National Laboratory, Oak Ridge, Tennessee, 37831-6123, is managed by UT-Battelle, LLC for the Department of Energy under Contract No. DE-AC05-0096OR22725.

APPENDIX A

The asymptotic form of the defined ratios

$$K_q^m(\mu) = \frac{P^m_{-(1/2)+iq}(\mu)}{P^m_{-(1/2)+iq}(-\mu)} \underset{q\gg 1}{\sim} e^{-q(\pi-2\theta)} \frac{8q\tan\theta - 4m^2 + 1}{8q\tan\theta + 4m^2 - 1}, \tag{A1}$$

$$\hat{K}_q^m(\mu) = \frac{\partial_\mu P^m_{-(1/2)+iq}(\mu)}{\partial_\mu P^m_{-(1/2)+iq}(-\mu)} \underset{q\gg 1}{\sim} e^{-q(\pi-2\theta)} \frac{3 - 8q\tan\theta}{3 + 8q\tan\theta}, \tag{A2}$$

$$\epsilon_q^m(\mu) = \frac{K_q^m(\mu)}{\hat{K}_q^m(\mu)} \underset{q\to\infty}{\longrightarrow} -1. \tag{A3}$$

Equations (A1) and (A2) evaluated at $\theta = \pi/2$

$$K_q^m(0) = 1, \quad \hat{K}_q^m(0) = -1, \quad \forall\, q,m. \tag{A4}$$

APPENDIX B

Functions $c_i^m(q)$ representing the coefficients of the polynomial (24)

$$c_0^m(q) = \epsilon_s \epsilon_t \lambda_q^m(\mu_c)\left[\hat{K}_q^m(\mu_t) - \frac{K_q^m(\mu_c)}{\varepsilon_q^m(\mu_t)}\right],$$

$$\begin{aligned} c_1^m(q) = {} & \hat{K}_q^m(\mu_t)\{\epsilon_t \overline{\Omega}_q^m(\kappa a) - \epsilon_s \lambda_q^m(\mu_c)[1 + \epsilon_t \zeta_q^m(\mu_c)]\} \\ & + \frac{\hat{K}_q^m(\mu_c)\epsilon_s \epsilon_t \lambda_q^m(\mu_c)\zeta_q^m(\mu_c)}{\varepsilon_q^m(\mu_t)} \\ & + K_q^m(\mu_c)\left[\epsilon_s \lambda_q^m(\mu_c) - \frac{\epsilon_t \overline{\Omega}_q^m(\kappa a)}{\varepsilon_q^m(\mu_t)}\right], \end{aligned}$$

$$\begin{aligned} c_2^m(q) = {} & \hat{K}_q^m(\mu_t)[\epsilon_t - \epsilon_t \Omega_q^m(\kappa a) - \overline{\Omega}_q^m(\kappa a) + \epsilon_s \lambda_q^m(\mu_c)\zeta_q^m(\mu_c)] \\ & + \hat{K}_q^m(\mu_c)\left[\frac{\epsilon_t \Omega_q^m(\kappa a)}{\varepsilon_q^m(\mu_t)} - \epsilon_s \lambda_q^m(\mu_c)\zeta_q^m(\mu_c)\right] \\ & + K_q^m(\mu_c)\left[\overline{\Omega}_q^m(\kappa a) - \frac{\epsilon_t}{\varepsilon_q^m(\mu_t)}\right], \end{aligned} \tag{B1}$$

$$\begin{aligned} c_3^m(q) = {} & \hat{K}_q^m(\mu_t)[\Omega_q^m(\kappa a) - \epsilon_t \overline{\zeta}_q^m(\mu_c) - 1] \\ & + \hat{K}_q^m(\mu_c)\left[\frac{\epsilon_t \overline{\zeta}_q^m(\mu_c)}{\varepsilon_q^m(\mu_t)} - \Omega_q^m(\kappa a)\right] \\ & + K_q^m(\mu_c), \end{aligned}$$

$$c_4^m(q) = \overline{\zeta}_q^m(\mu_c)[\hat{K}_q^m(\mu_t) - \hat{K}_q^m(\mu_c)],$$

where

$$\Omega_q^m(\kappa a) = \coth \kappa a[\lambda_q^m(\mu_c)\zeta_q^m(\mu_c) + \epsilon_s \overline{\zeta}_q^m(\mu_c)],$$

$$\overline{\Omega}_q^m(\kappa a) = \coth \kappa a[\epsilon_s + \lambda_q^m(\mu_c)]. \tag{B2}$$

APPENDIX C

$$d(k,\omega) = \frac{1}{2k_3} \times \ln - \frac{v_1 u_2 T_1 + u_1 v_2 T_2}{v_1 v_2 T_3 + u_1 u_2 T_4}, \tag{C1}$$

where

$$T_1 = u_N u_3 + v_N v_3 e^{2k_2 a'},$$

$$T_2 = u_N u_3 e^{2k_2 a} + v_N v_3 e^{2k_2(a+a')},$$

$$T_3 = u_N v_3 + v_N u_3 e^{2k_2 a'},$$

$$T_4 = u_N v_3 e^{2k_2 a} + v_N u_3 e^{2k_2(a+a')}, \tag{C2}$$

with the frequency-dependent functions

$$u_i = \epsilon_{i+1}(\omega)k_i + \epsilon_i(\omega)k_{i+1},$$

$$v_i = \epsilon_{i+1}(\omega)k_i - \epsilon_i(\omega)k_{i+1},$$

$$k_i(k,\omega) = \left[k^2 - \epsilon_i(\omega)\frac{\omega^2}{c^2}\right]^{1/2}, \quad i = 1, \ldots, N, \tag{C3}$$

where $i=1$ refers to the first medium, whereas $i=N$ denotes the last medium. This is equivalent to letting the (p polarization) reflectance $r_p(k,\omega) \to \infty$ for the entire system in Fig. 5, which results in a transcendental equation for the resonance modes of the system.[72] When computing (C1), the principal branch of the natural logarithm is selected as the argument is complex. Equation (C1), in the limit $a' \to 0$, $\epsilon_t \to 1.0$ (see Fig. 6) describes the dispersion of surface plasmons in the Kretschmann configuration, which for $\epsilon_g = 1.0$, $\epsilon_{tc} = \epsilon(\omega)$, and $c \to \infty$ $(k_i \to k)$ is given by

$$\epsilon^2(\omega) + \coth kd(\epsilon_s + 1.0)\epsilon(\omega) + \epsilon_s = 0. \tag{C4}$$

*Email address: passianan@ornl.gov

[1] D. Bohm and D. Pines, Phys. Rev. **82**, 625 (1951).

[2] R. H. Ritchie, Phys. Rev. **106**, 874 (1957).

[3] T. L. Ferrell, T. A. Callcott, and R. J. Warmack, Am. Sci. **73**, 344 (1985).

[4] R. C. Reddick, R. J. Warmack, and T. L. Ferrell, Phys. Rev. B **39**, 767 (1989).

[5] A. Liebsch, *Electronic Excitations at Metal Surfaces* (Plenum, New York, 1997).

[6] B. E. Sernelius, *Surface Modes in Physics* (Wiley-VCH, Berlin, 2001).

[7] A. D. Boardman, *Electromagnetic Surface Modes* (Wiley, New York, 1982).

[8] E. Kretschmann, T. L. Ferrell, and J. C. Ashley, Phys. Rev. Lett. **42**, 1312 (1979).

[9] F. Meriaudeau, T. R. Downey, A. Passian, A. Wig, and T. L. Ferrell, Appl. Opt. **37**, 8030 (1998).

[10] P. Royer, J. P. Goudonnet, R. J. Warmack, and T. L. Ferrell, Phys. Rev. B **35**, 3753 (1987).

[11] J. L. Bijeon, P. Royer, J. P. Goudonnet, R. J. Warmack, and T. L. Ferrell, Thin Solid Films **155**, L1 (1987).

[12] S. W. Kennerly, R. J. Warmack, and T. L. Ferrell, Oak Ridge National Laboratory Report No. ORNL/TM-9407, 1976 (unpublished).

[13] K. L. Kliewer and R. Fuchs, Phys. Rev. **144**, 495 (1966).

[14] K. L. Kliewer and R. Fuchs, Phys. Rev. **150**, 573 (1966).

[15] K. L. Kliewer and R. Fuchs, Phys. Rev. **153**, 498 (1967).

[16] E. N. Economou, Phys. Rev. **182**, 539 (1969).

[17] E. N. Economou and K. L. Ngai, *Aspects of the Study of Surfaces*, edited by I. Prigogine and S. A. Rice (Wiley, New York, 1974), Vol. XXVII, p. 265.

[18] C. E. Wheeler, E. T. Arakawa, and R. H. Ritchie, Oak Ridge National Laboratory Report No. ORNL/TM-5185, 1976 (unpublished).

[19] I. R. Hooper and J. R. Sambles, Phys. Rev. B **65**, 165432 (2002).

[20] M. Kreiter, S. Mittler, W. Knoll, and J. R. Sambles, Phys. Rev. B **65**, 125415 (2002).

[21] R. Ruppin, in *Electromagnetic Surface Modes*, edited by A. D. Boardman (Wiley, New York, 1982), p. 344.

[22] A. Moussiaux, A. Ronveaux, and A. Lucas, Can. J. Phys. **55**, 1423 (1977).

[23] R. N. Hall, J. Appl. Phys. **20**, 925 (1949).

[24] S. S. Martinos and E. N. Economou, Phys. Rev. B **28**, 3173 (1983).

[25] C. A. Pfeiffer, E. N. Economou, and K. L. Ngai, Phys. Rev. B **10**, 3038 (1974).

[26] U. Schröter and A. Dereux, Phys. Rev. B **64**, 125420 (2001).

[27] U. C. Fischer and D. W. Pohl, Phys. Rev. Lett. **62**, 458 (1989).

[28] J. Aizpurua, G. Hoffmann, S. P. Apell, and R. Berndt, Phys. Rev. Lett. **89**, 156803 (2002).

[29] I. I. Smolyaninov, A. V. Zayats, A. Gungor, and C. C. Davis, Phys. Rev. Lett. **88**, 187402 (2002).

[30] I. I. Smolyaninov, D. L. Mazzoni, J. Mait, and C. C. Davis, Phys. Rev. B **56**, 1601 (1997).

[31] M. Specht, J. D. Pedarnig, W. M. Heckl, and T. W. Hänsch, Phys. Rev. Lett. **68**, 476 (1992).

[32] P. Dawson, B. A. F. Puygranier, and J. P. Goudonnet, Phys. Rev. B **63**, 205410 (2001).

[33] J. R. Krenn, J. C. Weeber, A. Dereux, E. Bourillot, J. P. Goudonnet, B. Schider, A. Leitner, F. R. Aussenegg, and C. Girard, Phys. Rev. B **60**, 5029 (1999).

[34] J. C. Weeber, J. R. Krenn, A. Dereux, B. Lamprecht, Y. Lacroute, and J. P. Goudonnet, Phys. Rev. B **64**, 045411 (2001).

[35] A. Bouhelier, Th. Huser, H. Tamaru, H.-J. Güntherodt, D. W. Pohl, F. I. Baida, and D. Van Labeke, Phys. Rev. B **63**, 155404 (2001).

[36] A. Madrazo, M. Nieto-Vesperinas, and N. García, Phys. Rev. B **53**, 3654 (1996).

[37] J. R. Arias-Gonzaléz, M. Nieto-Vesperinas, and M. Lester, Phys. Rev. B **65**, 115402 (2002).

[38] J. A. Porto, P. Johansson, S. P. Apell, and T. López-Ríos, Phys. Rev. B **67**, 085409 (2003).

[39] J. P. Fillard, *Near Field Optics and Nanoscopy* (World Scientific, Singapore, 1996).

[40] R. M. Stöckle, Y. D. Suh, V. Deckert, and R. Zenobi, Chem. Phys. Lett. **318**, 131 (2000).

[41] B. E. Sernelius and P. Björk, Phys. Rev. B **57**, 6592 (1998).

[42] A. Passian, A. Wig, A. L. Lereu, F. Meriaudeau, T. Thundat, and T. L. Ferrell, Appl. Phys. Lett. **85**, 3420 (2004).

[43] T. L. Ferrell, Nucl. Instrum. Methods Phys. Res. B **96**, 483 (1995).

[44] T. L. Ferrell, Phys. Rev. B **50**, 14 738 (1994).

[45] P. Moon and D. E. Spencer, *Field Theory Handbook* (Springer-Verlag, Berlin, 1961).

[46] N. N. Lebedev, J. Appl. Math. Mech. **11**(2), 251 (1947).

[47] C. Flammer, *Spheroidal Wave Functions* (Stanford University Press, Stanford, 1956).

[48] L. W. Li, M. S. Leong, T. S. Yeo, P. S. Kooi, and K. Y. Tan, Phys. Rev. E **58**, 6792 (1998).

[49] I. N. Sneddon, *The Use of Integral Transform* (McGraw-Hill, New York, 1972).

[50] M. I. Zhurina and L. N. Karmazina, *Tables and Formulae for the Spherical Functions* $P^{m}_{-(1/2)+iq}(z)$ (Pergamon, New York, 1966).

[51] L. Robin, *Fonctions Spheriques de Legendre et Fonctions Spheroidales, T.I., T.II., T.III* (Gauthier-Villars, Paris, 1957–1959).

[52] N. N. Lebedev, *Special Functions and Their Applications* (Prentice-Hall, Englewood Cliffs, NJ, 1965).

[53] N. A. Belova and I. S. Ufliand, J. Appl. Math. Mech. **31**(1), 59 (1967).

[54] N. N. Lebedev and I. P. Skalskaia, J. Appl. Math. Mech. **30**(5), 889 (1966).

[55] N. K. Chukhrukidze, Zh. Vychisl. Mat. Mat. Fiz. **5**, 742 (1965).

[56] N. K. Chukhrukidze, Zh. Vychisl. Mat. Mat. Fiz. **6**, 61 (1966).

[57] I. S. Gradshteyn and I. M. Ryzhik, *Table of Integrals, Series, and Products* (Academic Press, New York, 1980).

[58] R. G. Van Nostrand, J. Math. Phys. **10**, 276 (1954).

[59] A. Passian, S. Kouchekian, and T. L. Ferrell (unpublished).

[60] K. S. Kölbig, Comput. Phys. Commun. **23**, 51 (1981).

[61] W. H. Press, B. P. Flannery, S. A. Teukolsky, and W. T. Vetterling, *Numerical Recipes* (Cambridge University Press, New York, 1986).

[62] M. I. Zhurina and L. N. Karmazina, *Tables of the Legendre Functions* $P_{-(1/2)+i\tau}(x)$, *Part I* (Pergamon, New York, 1964).

[63] M. I. Zhurina and L. N. Karmazina, *Tables of the Legendre Functions* $P_{-(1/2)+i\tau}(x)$, *Part II* (Pergamon, New York, 1965).

[64] E. D. Palik, *Handbook of Optical Constants of Solids* (Academic Press, Orlando, 1985).

[65] C. Kittel, *Introduction to Solid State Physics* (Wiley, New York, 1966).

[66] J. W. Little, T. L. Ferrell, T. A. Callcott, and E. T. Arakawa, Phys. Rev. B **26**, 5953 (1982).

[67] T. Kokkinakis and K. Alexopoulos, Phys. Rev. Lett. **28**, 1632 (1972).

[68] S. P. Apell, P. M. Echenique, and R. H. Ritchie, Ultramicroscopy **65**, 53 (1996).

[69] R. Gordon, A. G. Brolo, A. McKinnon, A. Rajora, B. Leathem, and K. L. Kavanagh, Phys. Rev. Lett. **92**, 037401 (2004).

[70] S. Y. Shieh, Phys. Rev. **172**, 1310 (1968).

[71] S. Y. Shieh, Z. Phys. **172**, 406 (1968).

[72] B. B. Dasgupta and A. Bagchi, Phys. Rev. B **19**, 4935 (1979).

[73] T. Nagao, T. Hildebrandt, M. Henzler, and S. Hasegawa, Phys. Rev. Lett. **86**, 5747 (2001).

[74] E. Kretschmann, Z. Phys. **241**, 313 (1971).

[75] A. Otto, Z. Phys. **216**, 398 (1968).

[76] E. A. Stern and R. A. Ferrel, Phys. Rev. **120**, 130 (1960).